

Low Latency GNN Accelerator for Quantum Error Correction

Alessio Cicero
ciceroa@chalmers.se
Chalmers University of Technology
and University of Gothenburg
Sweden

Luigi Altamura
altamura@chalmers.se
Chalmers University of Technology
and University of Gothenburg
Sweden

Moritz Lange
moritz.lange@gu.se
University of Gothenburg
Sweden

Mats Granath
mats.granath@gu.se
University of Gothenburg
Sweden

Pedro Trancoso
ppedro@chalmers.se
Chalmers University of Technology
and University of Gothenburg
Sweden

Abstract

Quantum computers have the potential to solve certain complex problems in a much more efficient way than classical computers. Nevertheless, current quantum computer implementations are limited by high physical error rates. This issue is addressed by Quantum Error Correction (QEC) codes, which use multiple physical qubits to form a logical qubit to achieve a lower logical error rate, with the surface code being one of the most commonly used.

The most time-critical step in this process is interpreting the measurements of the physical qubits to determine which errors have most likely occurred - a task called decoding. Consequently, the main challenge for QEC is to achieve error correction with high accuracy within the tight $1\ \mu\text{s}$ decoding time budget imposed by superconducting qubits. State-of-the-art QEC approaches trade accuracy for latency. In this work, we propose an FPGA accelerator for a Neural Network based decoder as a way to achieve a lower logical error rate than current methods within the tight time constraint, for code distance up to $d=7$.

We achieved this goal by applying different hardware-aware optimizations to a high-accuracy GNN-based decoder. In addition, we propose several accelerator optimizations leading to the FPGA-based decoder achieving a latency smaller than $1\ \mu\text{s}$, with a lower error rate compared to the state-of-the-art.

CCS Concepts

• **Hardware** → **Hardware accelerators; Quantum error correction and fault tolerance.**

Keywords

GNN, FPGA, Quantum error correction, QEC decoder accelerator

1 Introduction

Quantum computers have the potential to revolutionize several domains by offering computational speed-ups compared to the execution on classical machines. Notable examples are complex problems such as developing new chemical compounds [30, 35, 36] or evaluating the physical properties of new materials [5, 9]. However, today’s quantum devices remain fundamentally limited by the high error rate of their physical qubits [8]. Qubits are the fundamental unit of a quantum computer, and their value is represented as a complex value, with an amplitude and phase [38]. Physical

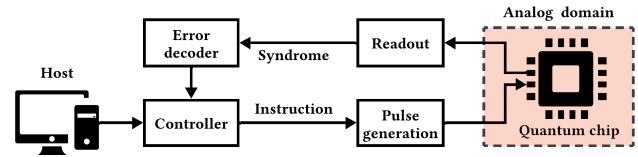


Figure 1: The host computer sends a quantum program to the controller, which drives the quantum chip with precise control pulses. The outputs of the chip are measured, and the error syndromes are computed from the observed errors. The controller may apply corrections based on those results.

qubits are highly susceptible to errors, which may take the form of bit flips or phase flips [38].

The error rate is defined as the gate execution time with respect to the lifetime of the qubit. A lower error rate thus allows for running an increased number of consecutive quantum gates. Current superconducting hardware have lifetimes on the order of a few hundred microseconds and gate times of the order a hundred nanoseconds, giving error rates on the order of 10^{-3} . Developing an effective implementation of quantum error-correction (QEC) [12] is necessary to support more complex algorithms, which may require millions or billions of gates, and move towards the era of fault-tolerant quantum computing (FTQC) [38].

Among the possible QEC codes proposed in the literature for superconducting qubits, the surface code [16] has emerged as one of the most promising approaches. This is due to its high threshold, corresponding to the physical qubit error rate below which increasing the number of qubits does not lead to a decrease in logical error rate, and its compatibility with two-dimensional qubit layouts typical of superconducting platforms [2]. The surface code encodes multiple physical qubits as a single logical qubit, allowing it to achieve an overall logical error rate lower than the error rate of the individual physical qubits. The number of physical qubits and therefore the logical error rate are connected to the code distance, which defines the size of the chosen surface code [16].

The decoding - process of identifying and correcting errors based on the graph generated from the measured errors - is the most time-critical operation of the QEC, as it is necessary to process each graph fast enough to avoid incurring in a backlog of measurements. The execution flow is shown in Figure 1.

In the case of the surface code for superconducting qubits [18], the maximum acceptable latency for the decoding is $1 \mu\text{s}$ [2], the latency of a round of measurements of the physical qubits.

Different algorithms have been consistently used to decode the surface code, each one with a different trade-off between latency and logical error rate. Most of the previous works on accelerators for real-time decoding develop either Minimum-Weight Perfect Matching (MWPM) [4, 47, 48] or Union Find (UF)-based decoders [15].

In our work, we decide to use a higher accuracy decoder based on a graph neural network (GNN) [28], which has been shown to outperform both MWPM and UF in terms of logical error rate compared to them for code distances equal to 3, 5 and 7.

In the context of single-inference for QEC, where each measurement must be decoded immediately upon error graph generation, software-based decoders are too slow to meet the latency constraint of $1 \mu\text{s}$. The most common approach to real-time decoding, as also shown in the previously mentioned works [4, 47, 48], is to design an FPGA-based accelerator optimized for single inference decoding. Motivated by these considerations, we develop an FPGA-based solution optimized specifically for single-inference GNN execution.

Starting from the GNN described in [28], whose architecture and experimental setup are fully specified and publicly available, we first analyze the trade-off introduced by reducing the number of layers using pruning-aware training, where improved latency is obtained at the expense of an increased logical error rate. We then design a hardware architecture optimized for single-inference latency. We achieve real-time decoding and a logical error rate of 1.47×10^{-5} , 13% lower compared to the MWPM, which approximately corresponds to enabling the execution of quantum circuits that are 13% longer at no additional physical-qubit cost.

Our key contributions include:

- An optimized version of the GNN-based decoder that maintains a logical error rate advantage with a $9\times$ reduction in the number of parameters.
- Multiple hardware-aware approaches, including post-training quantization, input-graph pruning, and hardware-informed architectural decisions, that allow for optimizing the use of the available hardware resources.
- A custom-designed FPGA-based hardware accelerator of the GNN, that achieves a 13% lower logical error rate compared to the MWPM software implementation and performs within the $1 \mu\text{s}$ threshold.

2 Background

Superconducting physical qubits currently exhibit high physical error rates (typically 10^{-3} [24]), far above what is tolerable for any useful applications of quantum algorithms. For example, factoring a 2048-bit RSA integer with Shor’s algorithm would require a logical error rate of 10^{-15} [21]. QEC achieves much lower logical error rates by encoding information using multiple physical qubits and correcting errors in real time. When combined with fault-tolerant gate implementations [41], QEC allows for increasing the number of sequential quantum computations carried out reliably, even in the presence of noise.

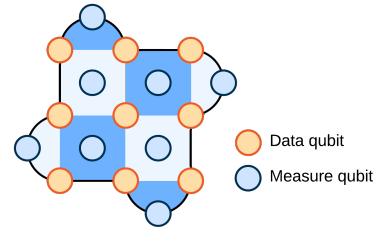


Figure 2: Surface code of distance 3, with qubits highlighted according to their roles as data or measurement qubits.

2.1 Quantum Error Correction

Quantum systems are inherently fragile due to their susceptibility to decoherence and noise from interactions with the environment.

Unlike classical bits, which can be easily stored and measured, qubits exist in superpositions of states and collapse upon measurement. Moreover, quantum information cannot be copied (as per the no-cloning theorem), which makes traditional error correction techniques unfeasible [38].

To preserve the integrity of the logical qubit, QEC protocols encode the logical information in a set of data qubits. Additional qubits (often referred to as ancilla qubits or measure qubits [16, 38]), are dedicated solely to measurement operations. These interact with the data qubits and are then measured to extract error syndromes: the outcomes of measurements that indicate which type of error (if any) occurred, without revealing or disturbing the encoded state. To quantify decoding performance, we can define the logical error rate as the proportion of correctly predicted logical errors out of the total number of syndromes:

$$\text{Logical error rate} = \frac{\text{Correct predictions}}{\text{Total syndromes}} \quad (1)$$

2.2 Surface Code

The surface code is one of the most prominent QEC codes due to its high error threshold, locality of measuring quantum circuits, and suitability for hardware with planar layouts and nearest-neighbor interactions, making it one of the leading candidates for practical fault-tolerant quantum computation. As shown in Figure 2, its underlying graph aligns well with the physical qubit connectivity of actual quantum hardware. [2].

Figure 2 illustrates the relationship between code distance (d) and the number of physical qubits used to encode a single logical qubit. Specifically, d^2 data qubits and $d^2 - 1$ measure qubits are required. Measurements are performed using dedicated quantum circuits, defining stabilizers [38], between the data qubits and the measure qubits. The surface code can correct up to $\lfloor \frac{d-1}{2} \rfloor$ single-qubit errors [16].

Lastly, to account for circuit-level noise, d repeated measurements are required to detect data qubit errors and also potential readout errors, with $d_t = d$. Multiple rounds of measurement help distinguish genuine changes in data qubit states from spurious results caused by noise affecting the measurement qubits or the readout process.

2.3 Decoding Algorithms

In QEC codes, physical errors manifest as changes in syndrome measurements. Decoding is the process of interpreting this syndrome to identify the most likely (logical) set of errors that occurred, preserving the encoded logical information.

Efficient and accurate decoding is critical for maintaining fault tolerance, especially under the stringent time constraints imposed by the quantum hardware.

A variety of decoding algorithms have been developed, each balancing trade-offs between accuracy, computational complexity, and suitability for hardware acceleration. The most common approaches are summarized here:

- **Union find decoder (UF)** [15]: A lightweight and low-complexity decoding algorithm, that yields higher logical error rate compared to the other more advanced methods.
- **Minimum weight perfect matching decoder (MWPM)** [27]: The most widely adopted decoder for surface codes. It offers improved accuracy over Union-Find but comes with higher computational complexity.
- **Belief propagation decoder (BP)** [39]: A more computationally intensive approach than MWPM, particularly suited for decoding quantum Low-Density-Parity-Check [11] codes, where MWPM is less effective.
- **Neural-network-based decoders (NN)** [10, 28, 45, 46]: These decoders offer a flexible design space, with accuracy and complexity varying widely depending on the model architecture and training methodology.

2.4 Related Work

The most commonly used decoder for hardware implementation is MWPM [4, 14, 47], with the current state-of-the-art being Micro Blossom [48]. The authors are able to decode surface codes of code distance up to $d = 13$ while still being under the $1 \mu\text{s}$ threshold, and fitting the hardware decoder in a single Xilinx Versal VMK180 FPGA. While they are able to achieve the required latency, the logical error rate of the MWPM approach is still worse than that obtainable from most neural-network approaches.

Another main line of work is on the UF decoding, which achieves reduced decoding complexity at the cost of increased logical error rates than MWPM. However, its simpler algorithm allows for an even faster execution. The state-of-the-art work implementing the UF decoder on FPGA is [34]; they are able to decode surface codes up to $d = 51$ while still achieving the real-time latency. While prioritizing lower-complexity decoders is important for maintaining low latency at higher code distances, high-accuracy decoders achieve lower logical error rates, with the same number of qubits, supporting more complex quantum circuits in the future. That is why in our work, we use the GNN decoder.

Multiple works [1, 25, 26, 37, 50, 51] present hardware acceleration of GNNs, but only a limited number of them focus on optimizing the single-inference latency for sub-microsecond FPGA execution. The only comparable work in terms of latency constraints we have knowledge of, Que et al. [42], also focuses on the sub-microsecond inference latency; however, their GNN is significantly smaller, with $\approx 3,000$ parameters. As a result, despite similar timing constraints, the design trade-offs and overall approaches

diverge, with their work emphasizing micro-architectural choices and ours focusing mainly on system-level optimizations.

3 GNN-based Decoder

The GNN decoder used in our work is based on the architecture proposed by Lange et al. [28], designed to decode surface code syndromes under realistic, circuit-level noise. The decoder treats each multiple rounds of stabilizer measurements as a graph, where nodes represent detection events and edges connect them based on local proximity. Each node is annotated with a feature vector encoding the stabilizer type (X or Z) and its space-time coordinate.

The network follows a message-passing paradigm composed of the following stages:

- **Input Encoding:** Each node starts with a feature vector $\vec{X}_i^{(0)} \in \mathbb{R}^5$ representing local information as discussed above.
- **Graph Convolution (GraphConv) Layers:** A sequence of L message-passing layers propagates information across the graph. Each layer ℓ updates node embeddings via:

$$\vec{X}_i^{\ell+1} = \sigma \left(W_1^\ell \vec{X}_i^\ell + W_2^\ell \sum_j e_{ij} \vec{X}_j^\ell + \vec{b}^\ell \right) \quad (2)$$

where W_1^ℓ , W_2^ℓ and \vec{b}^ℓ are the trainable weights of layer ℓ and the element-wise acting rectified linear unit, $\sigma(x) = \text{ReLU}(x) = \max(0, x)$.

- **Global Mean-Pooling (GMP):** After message passing, node embeddings are aggregated using mean-pooling to form a graph-level embedding:

$$\vec{X}_{\text{mean}} = N^{-1} \sum_i \vec{X}_i^L, \quad (3)$$

for a graph consisting of N nodes.

- **Classification Head:** A final multilayer perceptron composed of fully connected (dense) layers maps \vec{X}_{mean} to a binary output indicating the presence of a logical error.

The GNN operates on an input graph constructed from the measured syndrome data. Each syndrome measurement corresponds to a node in the graph. During graph construction, each node is connected to its k -nearest neighbors, forming an undirected graph. Each edge is assigned a weight, which is symmetric with respect to the direction and is computed as the inverse of the square Euclidean distance between the connected nodes. The resulting input graph consists of n nodes, where the maximum n depends on the code distance. Each node in the graph is characterized by the following components:

- **Node features:** Each node is associated with a feature vector of dimension 5, as the original GNN.
- **Edge indices:** A list that encodes graph connectivity by specifying source and target node pairs.
- **Edge weights:** A set of scalar weights for each edge, derived from the inverse square of the distance between nodes.

Although the software GNN decoder has a lower logical error rate than the MWPM one, as shown in Table 1, its single-graph inference time is one order of magnitude greater—far exceeding the latency requirements for real-time surface code decoding.

Table 1: Logical error rate and single batch inference time per cycle. Comparison between the GNN [28] and MWPM [22]. Experiment conducted on a system equipped with an Intel i9-12900K CPU and an NVIDIA RTX A4000 GPU.

Decoder	Logical error rate	Average inference time
MWPM [22]	1.69×10^{-5}	30.3 μ s
GNN [28]	8.27×10^{-6}	291.4 μ s

To achieve the low-latency requirements of our application, we transition to a custom hardware accelerator, similarly to prior work in the field [34, 47, 48]. Specifically, we adopt an FPGA-based implementation, which represents the state-of-the-art approach for this class of problems. This choice is further motivated by the fact that other critical components of the quantum stack—such as the quantum controller—are also typically implemented on FPGAs [49], enabling tighter integration and more efficient co-design.

4 GNN Hardware Implementation

As shown in Section 3, the software implementation of the GNN has a latency in the order of hundreds of microseconds even when executed on workstations, which is orders of magnitude slower than the required threshold. In this section, we present our hardware-aware co-design methodology, aimed at optimizing FPGA resource utilization to accommodate the GNN, while simultaneously reducing overall latency to meet the tight timing constraints.

Following a co-design approach, after a first evaluation of the upper bounds in terms of latency and resource utilization of a FPGA-based implementation of the GNN, we present multiple steps in the optimization of the system, from pruning the initial model to the design choices of the hardware implementation, aimed at achieving the required latency.

4.1 Bottleneck Characterization

The implementation of the previously described GNN in hardware is unfeasible in any currently available FPGA, due to the resource and latency constraints. As presented in Table 2, the number of parameters is in the order of millions, which presents a challenge in terms of computation latency. Additionally, as shown, the number of multiplications scales linearly with the number of nodes of the measured surface code graph.

This greatly increases the overall number of operations per layer, due to the fact that the maximum number of nodes in the input graph scales cubically with the code distance (d). This is because the number of measurements (d_t) is also equal to the code distance, such that $d = d_t$:

$$\max(N_{nodes}) = \frac{d^2 - 1}{2} \cdot d_t$$

Respectively, for $d = 3, 5,$ and 7 the maximum number of nodes is 12, 60, and 168.

Assuming the worst-case for $d = 7$, we can have up to 168 input nodes, leading to a number of multiplications in the order of 10^8 . Considering an average FPGA $f_{clk} = 300MHz$, and the required maximum latency of 1μ s, we would need to process $\approx 3 \cdot 10^6$

Table 2: Number of multiplications required for each layer of the GNN of the work [28]. GraphConv layers are reported as a function of the number of nodes n of the input graph.

Layer	d_{in}	d_{out}	Multiplications
GraphConv ₀	5	32	$320 \times n$
GraphConv ₁	32	128	$8,192 \times n$
GraphConv ₂	128	256	$65,536 \times n$
GraphConv ₃	256	512	$262,144 \times n$
GraphConv ₄	512	512	$524,288 \times n$
GraphConv ₅	512	256	$262,144 \times n$
GraphConv ₆	512	256	$131,072 \times n$
GMP	256	256	256
Dense ₀	256	256	65,536
Dense ₁	256	128	32,768
Dense ₂	128	64	8,192
Dense _{out}	64	1	64

operations per cycle. As this is too high for today’s FPGA, it is necessary to optimize the implementation at multiple levels.

4.2 Hardware-Aware Pruning

A first evaluation of the distribution of the values of each layer output feature vector, after running the GNN inference on 10^8 input graphs, highlighted how many output features had a high probability of being zero, due to the ReLU nonlinearities. This distribution is element-specific, with certain vector elements exhibiting a higher probability of being zero. Finally, some of the layers presented a greater number of elements in the output feature vector compared to the others. In Table 3 we report the number of the output vector feature elements of each layer that are zero with at least an 80% probability, which we define as the activation sparsity probability.

This insight led us to examine the impact of pruning layers with the highest activation sparsity on the logical error rate, under the hypothesis that pruning these layers would incur only a minimal degradation in error-correction performance. This observation is particularly significant, as the layers with the greatest number of prunable elements are also the most multiplication-intensive, thereby yielding a larger optimization benefit.

We determine the pruning order by ranking layers based on their number of avoidable multiplications, defined as the product of the activation sparsity probability and the layer’s total multiplication count. Reducing the number of layers, and thus the number of parameters, yields significant reductions in latency and storage, at the cost of a possible increase in the logical error rate.

Since post-training pruning [6, 7, 17, 23, 31, 33, 44] - removing layers without retraining - resulted in a substantial increase in the logical error rate, we instead adopt pruning-aware training [13, 29, 32, 43] - by retraining the GNN after pruning. Retraining is performed after initializing the remaining layers with the unpruned model weights, as this approach was observed in initial tests to converge more quickly to the original logical error rate.

4.3 Input Graph Optimization

After the number of layers, the second most impactful parameter on the total number of operations is the maximum supported input

Table 3: Layer-wise sparsity of GraphConv layers across different code distances, defined as the fraction of features that are zero at least 80% of the time after ReLU. Avoidable multiplies column is the number of potential savings in number of multiplications due to stuck on zero output features in the case of $d = 7$.

Layer	d3	d5	d7	Avoidable Multiplies
GraphConv ₀	28%	28%	31%	$100 \times n$
GraphConv ₁	24%	34%	28%	$2,304 \times n$
GraphConv ₂	58%	54%	49%	$32,000 \times n$
GraphConv ₃	65%	70%	54%	$141,312 \times n$
GraphConv ₄	66%	71%	67%	$351,232 \times n$
GraphConv ₅	57%	70%	73%	$190,464 \times n$
GraphConv ₆	91%	87%	88%	$115,200 \times n$

graph size, as the overall computational cost scales linearly with the number of nodes. This is because each graph convolution layer applies the same operations to every node, as previously shown in Equation 2 and Table 2.

By evaluating if it is necessary to consider the worst-case scenario in terms of maximum nodes supported, and possibly optimizing it, it is possible to significantly reduce the total number of iterations. By bounding the input graph size according to the maximum number of nodes that must be supported, and discarding rarer, more complex graphs that have negligible impact on the final logical error rate, we can significantly reduce overall latency. We therefore evaluate the statistics of the input graph in 5.3.

4.4 Post-Training Quantization

The bitwidth of the weights and each layer’s output features directly affects resource utilization and computation latency. The allocation of the available Block RAMs (BRAMs), Digital Signal Processors (DSPs), Flip-flops (FFs), and Look-up tables (LUTs) can be significantly optimized by evaluating and optimizing the bitwidth of the different parts of the system. Since the number of required operations and stored parameters remains significant even after layer pruning and input graph optimization, further system-level optimization is necessary. To identify the optimal bitwidth for the different parts of the system, we conducted a more detailed design space exploration, with a post-training quantization [19] of output features, weights, and biases of the GNN.

Because the GNN output is followed by a sigmoid function, we study the effect of aggressive quantization on the logical error rate and identify the minimum precision that does not affect performance, which we define as the optimal quantization.

We first evaluate output features, weight, and bias quantization independently by applying fixed-point formats to one component at a time while keeping the others in single-precision floating point. We then combine the optimal configurations and evaluate joint quantization of all three components. Although the quantization effects across components are not independent, combining the optimal configurations of each component provides a practical and effective starting point for the joint evaluation, significantly reducing the design space and avoiding a combinatorial explosion.

4.5 Hardware Implementation and Architectural Optimizations

In Figure 3 we present our architecture. It is a three-pipeline-stage architecture. Upon receiving a new syndrome, node and edge features are stored in registers. Each layer is processed sequentially in one or more cycles.

4.5.1 Input selection. In this stage, we select the node(s) that will be computed in the following stages. In the first cycle of each new layer, we forward the updated nodes from the output node register. For the graph_conv layers, the computation strategy is selected based on the number of multiplications required per node: we process either multiple nodes in parallel, a single node together with the precomputed aggregated neighbors, or only one of the two. In the latter case, the computation may be further split across multiple cycles by partitioning the computations of the output features when required. The aggregated neighbours, defined as the product of the edge weights and the neighbours of each node, need to be computed before each node execution.

The GMP layer is implemented by first accumulating each feature element across all nodes and then normalizing the result by the number of nodes. Accordingly, we introduce a dedicated adder tree in the first pipeline stage.

For dense layers, the graph was reduced to a single node; however, the computation of the output features may still be split across multiple cycles, based on the required number of multiplications.

4.5.2 Multipliers stage. In this stage, since multiplication is the dominant operation in each layer, we instantiate a multiplier array sized to the available DSP resources. Mapping multiplications directly to DSPs is essential, as exceeding the available DSP resources causes multipliers to be implemented in LUTs, leading to a rapid increase in LUT utilization and eventual overutilization.

If the number of available DSPs is less than the maximum number of computations required for some layers, we apply folding [40]. By partitioning the output columns into groups and computing one group per cycle, we ensure that the number of multiplications executed per cycle matches the available number of DSPs.

In the graph_conv layers, the multipliers compute the product between the neighbor nodes and the edge weights, the current node and the node feature weights matrix, or the aggregated neighbors and the node neighbor feature matrix. In the GMP layer, the accumulated features are normalized by multiplying each feature element by a normalization factor stored in the weights BRAMs, which depends on the number of nodes. In the case of the dense layer, we compute the product between the input features and the weights matrix, or part of it, based on the size of the layer. The first dense layer Multipliers stage cycle uses the GMP layer feed-forwarded output from the following stage. Two of the adder tree stages used for the reduction of the output of the graph_conv and dense layers are computed already in this stage, as the final adder tree critical path, the longest critical path in the architecture, has been divided between the two stages to reduce the maximum latency.

4.5.3 Adder tree stage. This stage contains the remaining stages of the adder tree. As described above, graph_conv is executed in two phases: the self contribution, including bias addition, is computed and stored first, followed by computation and accumulation of the

neighbor contribution. In dense layers, the bias is always added during the final accumulation. As several layers have a compatible output shape, we optimize the number of adder trees required, based on the final pruned GNN architecture. The GNN final output requires a final sigmoid activation function to obtain the result.

4.5.4 Other design choices and optimizations. Starting from the initial architecture, we describe the multiple optimized design choices that aim at either reducing the computation latency or resource utilization. Importantly, this level of customization does not restrict our design to a specific FPGA model. The architecture is fully parametrized with respect to the available DSP resources, enabling portability across different platforms.

Interleaved edge computation. Computing the graph_conv layers requires first computing the product between the edge weights and the selected node neighbors. As the number of multiplications required for this step is non-negligible, we need to use the multiplication kernel to allow for maximum parallelism. To save some cycles, we can first compute multiple aggregated neighbors at the same time, and secondly, we can move the computation of the new nodes to two cycles before the end of the current batch of nodes, as due to the pipelining, the new aggregated neighbors’ value will not be saved until the new node computation starts.

Weight and Bias Storage. Weights are stored in the available BRAMs. To maximize parallel computation, each cycle must supply a number of weights equal to the maximum number of concurrent multiplications. Multiple weights are packed into each memory address, and the weights stored in the BRAMs are organized such that, in each multiplication cycle, all required weights can be accessed by reading the same address across multiple parallel BRAMs.

Global Mean-Pooling Division. To eliminate expensive runtime division in the GMP operation, we replace the division with pre-computed normalization factors stored in the BRAMs alongside the weights. Because much of the BRAMs address space is unused, these scaling factors are placed at a dedicated base address, and the input graph count is used as an address offset to select the appropriate factor. Although this does not affect the latency directly, it reduces the number of multiplexers needed to control the input of the DSPs, allowing the design to meet the stringent LUT budget.

5 Evaluation

In this section, we evaluate the performance of the hardware implementation of our optimized GNN. We assess the impact of each optimization described in Section 4 on the FPGA-based GNN complexity, decoding latency, and overall logical error rate. Among the three evaluated distances, $d = 7$ is the most sensitive to design variations and the most computationally demanding due to its larger graph size; moreover, its higher code distance results in a lower logical error rate, making it the most significant case. Therefore, we will focus on the evaluation and design for code distance $d = 7$.

5.1 Evaluation setup

The evaluation of the reported logical error rates has been done with simulated syndrome measurements generated by Stim [20], with circuit-level noise model, physical error rate of $p = 10^{-3}$, sample

Table 4: Alveo U280 resources summary

LUT	FF	BRAM	DSP
1,303,680	2,607,360	2016	9024

Table 5: Number of multiplications required for each layer of the GNN. GraphConv layers are reported as a function of the number of nodes n of the input graph.

Layer	Multiplications
GraphConv ₀	$320 \times n$
GraphConv ₁	$8192 \times n$
GraphConv ₂	$32768 \times n$
GMP	256
Dense ₀	65536
Dense ₁	32768
Dense ₂	8192
Dense _{out}	64

size of 10^8 for $d = 7$, and sample size of 10^7 for $d=3, 5$, coherently with the evaluation of the GNN [28] we selected for our work.

The GNN and MWPM [22] software decoder inference time shown in Table 1 have been computed on a system equipped with an Intel i9-12900K CPU and an NVIDIA RTX A4000 GPU.

The GNN training has been run on a cluster with nodes equipped with Intel(R) Xeon(R) Gold 6338 CPU and NVIDIA Tesla A40 GPU. The FPGA-based decoder is designed in VHDL, and is designed using Vivado 2023.1, targeting the Xilinx Alveo U280 FPGA (device model: xcu280-fsvh2892-2L-e), a commercially available, high-end accelerator card. The FPGA resources are summarised in Table 4. We chose the U280 as it is representative of modern FPGAs in terms of logic capacity, memory bandwidth, and on-chip resources. For latency, we consistently report the single-inference latency, as previously defined in the background section.

5.2 Pruning-Aware Training

Starting from the original GNN, we evaluate different configurations with an increasing number of pruned layers. The different configurations are shown in Figure 4, the reported logical error rate refers to the case of $d = 7$.

The number of training epochs (training cycles) differs across configurations. While the three most complex pruned configurations have been retrained for 1,000 epochs, the smallest network has been retrained extensively for 5,000 epochs. This is because after an initial evaluation of the possible configurations and of the available resources, also based on the other optimizations, we picked the model with the layers graph_conv4, graph_conv5, graph_conv3, graph_conv6, pruned and additionally we pruned the 50% features with the highest activation sparsity. Retraining was done until the model no longer showed an improvement of at least 1% in logical error rate after 100 training epochs. This final configuration still maintains an advantage over the MWPM logical error rate of 1.34×10^{-5} , while greatly reducing the number of parameters and required multiplications, as shown in Table 5.

This choice allows to reduce the total number of parameters from 1.4×10^7 to 1.5×10^6 , while still maintaining for $d = 3, 5$, and

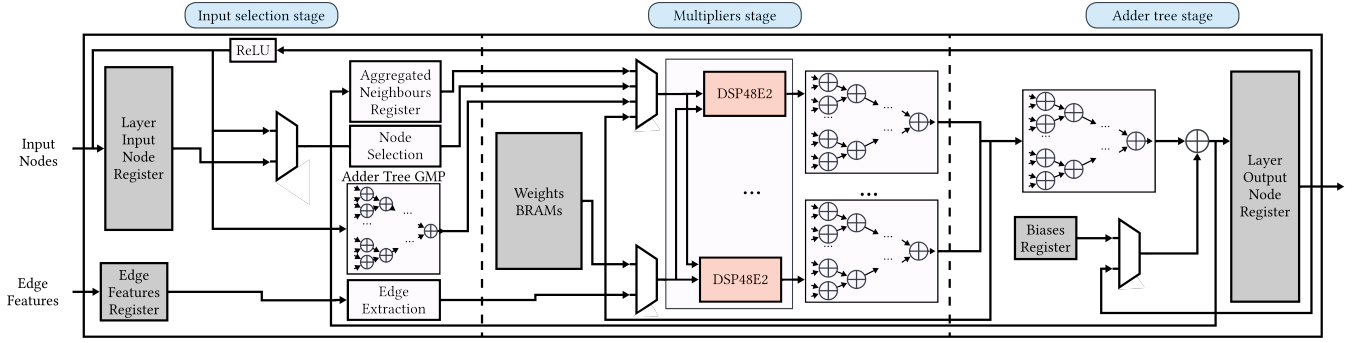


Figure 3: Three pipeline stages architecture of the GNN.

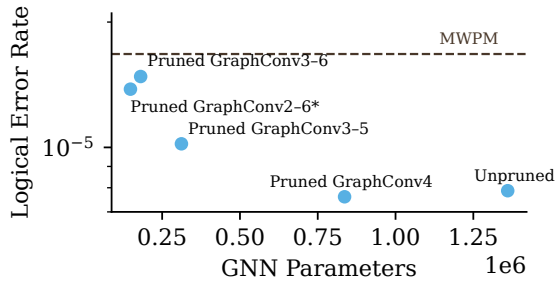


Figure 4: Comparison between the different logical error rates and number of parameters of different configurations pruned and retained for code distance $d = 7$. *Note: Layer graph_conv2 is not entirely pruned, but half of its outputs are computed, and has been retrained for $5\times$ more epochs compared to the other configurations.

7 respectively a 22%, 51%, and 21% advantage in terms of logical error rate over the MWPM decoder.

5.3 Input-Graph Optimization

We analyze the distribution of the number of nodes in the input graph, as shown in Figure 5.

As shown in the chart, the probability of having graphs with a number of nodes equal to or higher than 31, is $\approx 1.2 \times 10^{-6}$ for $d = 7$, which is more than an order of magnitude lower than the GNN logical error rate, 8.27×10^{-6} . This implies that the probability of encountering an error due to an unsupported, overly large graph is lower than the target logical error rate. We can therefore limit the input size of the graphs and consider a better-than-worst-case scenario in terms of execution time and required hardware.

Considering a smaller number of maximum nodes leads to a saving of up to 82% of the total number of multiplications, retaining a logical error rate advantage over MWPM of 19%. Both code distances $d = 5$ and $d = 3$ are unaffected: for $d = 5$, the probability of input graphs exceeding 30 nodes is several orders of magnitude lower than the target logical error rate, while for $d = 3$ the value 30 exceeds the maximum possible number of nodes.

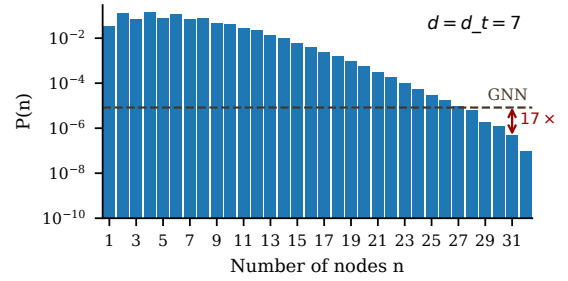


Figure 5: GNN input graph node count probability distribution for code distance $d = 7$, where $P(n)$ denotes the probability that an input graph contains n nodes.

5.4 Post-Training Quantization

The results of the post-training quantization independently applied to weight, bias, and output features of the model are shown in Figure 6. While bias and weights can still achieve the same logical error rate as the unquantized model, the quantization of the output features leads to a loss. After a design space exploration of the fully quantized model based on the previous analysis, we observed that the best quantization settings that optimize resource usage, reduce resource latency, and minimize logical error rate loss are the following:

- Weights quantized to 14-bit fixed-point with 4 integer bits and 10 fractional bits,
- Output features quantized to 17-bit fixed-point with 12 integer bits and 5 fractional bits,
- Biases quantized to 5-bit fixed-point with 1 integer bits and 4 fractional bits.

We keep biases at the same quantization as the data, as more aggressive quantization provides little benefit in terms of resource usage. This is due to the limited number of bias values and the requirement to extend them to the data precision during accumulation.

This allows us to optimize resource utilization. The primary gain comes from reducing the DSP usage per multiplication from four, as required for 32-bit operands, to one. While Alveo U280 DSPs support 48-bit inputs, the maximum bitwidth of one input port is 18 bits. As a result, mapping one multiplication per DSP allows a

Table 6: Number of clock cycles and latency required for each layer in case of $d = 7$, $n = 30$, and $t_{clk} = 4.8$ ns.

Layer	Clock Cycles	Latency [ns]
GraphConv ₀	7	33.6
GraphConv ₁	38	182.4
GraphConv ₂	137	657.6
GMP	2	9.6
Dense ₀	10	48
Dense ₁	6	28.8
Dense ₂	3	14.4
Dense _{out}	3	14.4
Total	206	988.8

4× increase in parallel multiplications. It also leads to a decrease in the maximum latency of the adder tree. After quantization, the advantage over MWPM is 13% for $d = 7$. With the same configuration, we retain 22% and 51% for $d = 3, 5$.

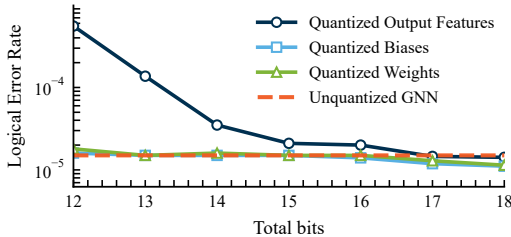


Figure 6: Effect of weights, layers output features, or biases only quantization on the logical error rate for code distance $d = 7$.

5.5 Hardware optimizations

Adder trees. Based on the chosen pruned architecture, by using the 256 32-input adder trees generated already for graph_conv1, we can save most of the operations for the other layers but graph_conv0. Although this does not affect the overall latency, it strongly affects the overall LUT utilization.

BRAMs organization. Based on the quantization results, we pack five 14-bit weights into each memory address. Supporting 8,192 parallel multiplications, therefore, requires reading an equal number of weights per cycle, which corresponds to accessing 1,639 BRAMs out of the 2,016 available. Although this represents a high fraction of the available BRAMs, the utilization of each BRAM’s address space remains low, leaving sufficient capacity to store the GMP normalization factors as discussed earlier. Bias values, by contrast, are stored directly in registers due to their limited count. The final cycle count for the worst case with $n = 30$ is reported in Table 6.

5.6 Summary

We report the synthesis results in Table 7 and the optimizations and their effects in Figure 7. The latest node includes the final optimization at the hardware level to reach the sub-microsecond threshold, as the total number of cycles is 206, we can therefore achieve a total latency of 988.8 ns. We are therefore able to implement the GNN on

Table 7: Synthesis result of the FPGA decoder for Alveo U280.

LUT	FF	BRAM	DSP	t_{clk}
96.22%	15.09%	81.27%	90.78%	4.8 ns

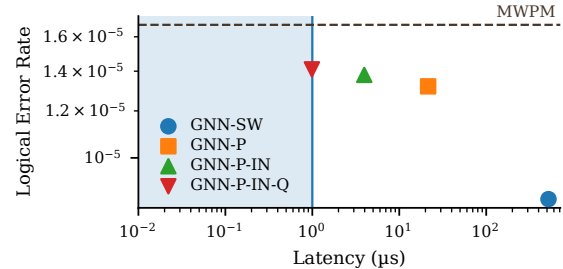


Figure 7: Comparison of logical error rate and latency across different GNN implementations: original GNN (GNN-SW), pruned GNN (GNN-P), pruned GNN with reduced maximum input nodes (GNN-P-IN), and pruned GNN with reduced maximum input nodes and quantization (GNN-P-IN-Q).

the FPGA within the available resources and latency, with a logical error rate of 6.10×10^{-4} , 7.36×10^{-5} , and 1.47×10^{-5} respectively for $d = 3, 5$, and 7 .

5.7 Discussion

Further improvements to the decoder can be achieved either by accommodating a less aggressively pruned model, thereby reducing the logical error rate, or by supporting larger code distances. Both directions require an increase in hardware resources. In the former case, additional memory capacity and greater parallelism are needed to sustain the larger model. In the latter, scaling to higher code distances primarily demands increased parallelism to offset the additional cycles required to process the larger number of nodes. Although the selected FPGA is close to full resource utilization, current and future FPGAs, such as the Xilinx Versal series, provide additional DSP, LUT, and BRAM resources that can be exploited in several ways. Increased compute and memory capacity enables greater parallelism, reducing per-layer latency and allowing less aggressive pruning, which can further improve the logical error rate relative to MWPM. Additional resources also support scaling to larger code distances, where worst-case error patterns substantially increase the number of nodes and operations per layer. Moreover, as QEC methodologies continue to evolve, alternative decoding models such as Google’s approach of defining the decoding deadline as d_t cycles introduce more relaxed timing constraints that can be leveraged to reduce logical error rates [3]. Under these conditions, we would be able to run a different configuration of the initial GNN in which two layers are fully pruned, and one layer is partially pruned, maintaining the logical error rate of the original GNN decoder while achieving a latency of $7 \mu s$. We would be able to then achieve the initial 51% advantage in terms of logical error rate compared to the MWPM.

6 Conclusion

In this work, starting from a software-based GNN, we applied several hardware-oriented optimizations to be able to execute real-time QEC. Pruning-aware training, input graph-pruning, post-training quantization, and multiple hardware-level design choices targeting the optimal usage of the resources and latency reduction. By applying these optimizations, we achieve a worst-case latency for $d = 7$ of 988.8 ns per inference with a logical error rate of 1.47×10^{-5} , retaining a 13% advantage over the MWPM, demonstrating the feasibility of deploying GNNs in low-latency, resource-constrained environments. Lastly, while our design choices are guided by hardware considerations, they remain broadly applicable and are not tied to the limitations of a specific FPGA.

Acknowledgments

We acknowledge support from the Swedish Foundation for Strategic Research (grant number FUS21-0063).

References

- [1] Stefan Abi-Karam and Cong Hao. 2023. Gnnbuilder: An automated framework for generic graph neural network accelerator generation, simulation, and optimization. In *2023 33rd International Conference on Field-Programmable Logic and Applications (FPL)*. IEEE, 212–218.
- [2] Google Quantum AI. 2023. Suppressing quantum errors by scaling a surface code logical qubit. *Nature* 614, 7949 (2023), 676–681.
- [3] Google Quantum AI. 2025. Quantum error correction below the surface code threshold. *Nature* 638, 8052 (2025), 920–926.
- [4] Narges Alavisamani, Suhas Vittal, Ramin Ayanzadeh, Poulami Das, and Moinuddin Qureshi. 2024. Promatch: Extending the Reach of Real-Time Quantum Error Correction with Adaptive Predecoding. In *Proceedings of the 29th ACM International Conference on Architectural Support for Programming Languages and Operating Systems, Volume 3*, 818–833.
- [5] Yuri Alexeev, Maximilian Amsler, Marco Antonio Barroca, Sanzio Bassini, Torey Battelle, Daan Camps, David Casanova, Young Jay Choi, Frederic T Chong, Charles Chung, et al. 2024. Quantum-centric supercomputing for materials science: A perspective on challenges and future directions. *Future Generation Computer Systems* 160 (2024), 666–710.
- [6] Yongqi An, Xu Zhao, Tao Yu, Ming Tang, and Jinqiao Wang. 2024. Fluctuation-based adaptive structured pruning for large language models. In *Proceedings of the AAAI Conference on Artificial Intelligence*, Vol. 38. 10865–10873.
- [7] Saleh Ashkboos, Maximilian L Croci, Marcelo Gennari do Nascimento, Torsten Hoefler, and James Hensman. 2024. Slicept: Compress large language models by deleting rows and columns. *arXiv preprint arXiv:2401.15024* (2024).
- [8] Francesco Battistel, Christopher Chamberland, Kausar Johar, Ramon WJ Overwater, Fabio Sebastiano, Luka Skoric, Yosuke Ueno, and Muhammad Usman. 2023. Real-time decoding for fault-tolerant quantum computing: Progress, challenges and outlook. *Nano Futures* 7, 3 (2023), 032003.
- [9] Bela Bauer, Sergey Bravyi, Mario Motta, and Garnet Kin-Lic Chan. 2020. Quantum Algorithms for Quantum Chemistry and Quantum Materials Science. *Chemical Reviews* 120, 22 (2020), 12685–12717. [arXiv:https://doi.org/10.1021/acs.chemrev.9b00829](https://doi.org/10.1021/acs.chemrev.9b00829) doi:10.1021/acs.chemrev.9b00829
- [10] Johannes Bausch, Andrew W Senior, Francisco JH Heras, Thomas Edlich, Alex Davies, Michael Newman, Cody Jones, Kevin Satzinger, Murphy Yuezhen Niu, Sam Blackwell, et al. 2023. Learning to decode the surface code with a recurrent, transformer-based neural network. *arXiv preprint arXiv:2310.05900* (2023).
- [11] Nikolas P Breuckmann and Jens Niklas Eberhardt. 2021. Quantum low-density parity-check codes. *Prx Quantum* 2, 4 (2021), 040101.
- [12] Avimta Chatterjee, Koustubh Phalak, and Swaroop Ghosh. 2023. Quantum error correction for dummies. In *2023 IEEE International Conference on Quantum Computing and Engineering (QCE)*, Vol. 1. IEEE, 70–81.
- [13] Tianyi Chen, Luming Liang, Tianyu Ding, Zhihui Zhu, and Ilya Zharkov. 2023. Otov2: Automatic, generic, user-friendly. *arXiv preprint arXiv:2303.06862* (2023).
- [14] Poulami Das, Aditya Locharla, and Cody Jones. 2022. Lilliput: a lightweight low-latency lookup-table decoder for near-term quantum error correction. In *Proceedings of the 27th ACM International Conference on Architectural Support for Programming Languages and Operating Systems*. 541–553.
- [15] Nicolas Delfosse and Naomi H Nickerson. 2021. Almost-linear time decoding algorithm for topological codes. *Quantum* 5 (2021), 595.
- [16] Austin G Fowler, Matteo Mariantoni, John M Martinis, and Andrew N Cleland. 2012. Surface codes: Towards practical large-scale quantum computation. *Physical Review A—Atomic, Molecular, and Optical Physics* 86, 3 (2012), 032324.
- [17] Elias Frantar and Dan Alistarh. 2022. Optimal brain compression: A framework for accurate post-training quantization and pruning. *Advances in Neural Information Processing Systems* 35 (2022), 4475–4488.
- [18] Jay M Gambetta, Jerry M Chow, and Matthias Steffen. 2017. Building logical qubits in a superconducting quantum computing system. *npj quantum information* 3, 1 (2017), 2.
- [19] Amir Gholami, Sehoon Kim, Zhen Dong, Zhewei Yao, Michael W. Mahoney, and Kurt Keutzer. 2021. A Survey of Quantization Methods for Efficient Neural Network Inference. [arXiv:2103.13630 \[cs.CV\]](https://arxiv.org/abs/2103.13630) <https://arxiv.org/abs/2103.13630>
- [20] Craig Gidney. 2021. Stim: a fast stabilizer circuit simulator. *Quantum* 5 (July 2021), 497. doi:10.22331/q-2021-07-06-497
- [21] Craig Gidney. 2025. How to factor 2048 bit RSA integers with less than a million noisy qubits. *arXiv preprint arXiv:2505.15917* (2025).
- [22] Oscar Higgott. 2022. Pymatching: A python package for decoding quantum codes with minimum-weight perfect matching. *ACM Transactions on Quantum Computing* 3, 3 (2022), 1–16.
- [23] Itay Hubara, Brian Chmiel, Moshe Isard, Ron Banner, Joseph Naor, and Daniel Soudry. 2021. Accelerated sparse neural training: A provable and efficient method to find n: m transposable masks. *Advances in neural information processing systems* 34 (2021), 21099–21111.
- [24] Petar Jurcevic, Ali Javadi-Abhari, Lev S Bishop, Isaac Lauer, Daniela F Bogorin, Markus Brink, Lauren Capelluto, Oktay Günlük, Toshinari Itoko, Naoki Kanazawa, Abhinav Kandala, George A Keefe, Kevin Krsulich, William Landers, Eric P Lewandowski, Douglas T McClure, Giacomo Nannicini, Adinath Narasgond, Hasan M Nayfeh, Emily Pritchett, Mary Beth Rothwell, Srikanth Srinivasan, Neereja Sundaresan, Cindy Wang, Ken X Wei, Christopher J Wood, Jeng-Bang Yau, Eric J Zhang, Oliver E Dial, Jerry M Chow, and Jay M Gambetta. 2021. Demonstration of quantum volume 64 on a superconducting quantum computing system. *Quantum Science and Technology* 6, 2 (March 2021), 025020. doi:10.1088/2058-9565/abe519
- [25] Geon-Woo Kim, Donghyun Kim, Jeongyoon Moon, Henry Liu, Tarannum Khan, Anand Iyer, Daehyeok Kim, and Aditya Akella. 2025. OMEGA: A Low-Latency GNN Serving System for Large Graphs. *arXiv preprint arXiv:2501.08547* (2025).
- [26] Taehwan Kim, Yunki Han, Seohye Ha, Jiwan Kim, and Lee-Sup Kim. 2025. EOD: Enabling Low Latency GNN Inference via Near-Memory Concatenate Aggregation. In *Proceedings of the 52nd Annual International Symposium on Computer Architecture*. 1125–1139.
- [27] Vladimir Kolmogorov. 2009. Blossom V: a new implementation of a minimum cost perfect matching algorithm. *Mathematical Programming Computation* 1 (2009), 43–67.
- [28] Moritz Lange, Pontus Havström, Basudha Srivastava, Isak Bengtsson, Valdemar Bergentall, Karl Hammar, Olivia Heuts, Evert van Nieuwenburg, and Mats Granath. 2025. Data-driven decoding of quantum error correcting codes using graph neural networks. *Physical Review Research* 7, 2 (May 2025). doi:10.1103/physrevresearch.7.023181
- [29] Namhoon Lee, Thalayasingam Ajanthan, Stephen Gould, and Philip HS Torr. 2019. A signal propagation perspective for pruning neural networks at initialization. *arXiv preprint arXiv:1906.06307* (2019).
- [30] Seunghoon Lee, Joonho Lee, Huanchen Zhai, Yu Tong, Alexander M Dalzell, Ashutosh Kumar, Phillip Helms, Johnnie Gray, Zhi-Hao Cui, Wenyuan Liu, et al. 2023. Evaluating the evidence for exponential quantum advantage in ground-state quantum chemistry. *Nature communications* 14, 1 (2023), 1952.
- [31] Chenhao Li, Lin Li, Zhibin Zhang, Qiang Qiu, Jiafeng Guo, and Xueqi Cheng. 2025. Improving Post-training Structured Pruning via Two-stage Reconstruction. *Expert Systems with Applications* (2025), 128930.
- [32] Junjie Liang, Lei Zhang, Can Bu, Dongzhou Cheng, Hao Wu, and Aiguo Song. 2024. An automatic network structure search via channel pruning for accelerating human activity inference on mobile devices. *Expert Systems with Applications* 238 (2024), 122180.
- [33] Gui Ling, Ziyang Wang, and Qingwen Liu. 2024. Slimpt: Layer-wise structured pruning for large language models. *Advances in Neural Information Processing Systems* 37 (2024), 107112–107137.
- [34] Namitha Liyanage, Yue Wu, Siona Tagare, and Lin Zhong. 2024. FPGA-based distributed union-find decoder for surface codes. *IEEE Transactions on Quantum Engineering* (2024).
- [35] Sam McArdle, Suguru Endo, Alán Aspuru-Guzik, Simon C. Benjamin, and Xiao Yuan. 2020. Quantum computational chemistry. *Reviews of Modern Physics* 92 (Mar 2020), 015003. Issue 1. doi:10.1103/RevModPhys.92.015003
- [36] Mario Motta and Julia E Rice. 2022. Emerging quantum computing algorithms for quantum chemistry. *Wiley Interdisciplinary Reviews: Computational Molecular Science* 12, 3 (2022), e1580.
- [37] Marc Neu, Christian Karle, Patrick Schmidt, Julian Höfer, Tanja Harbaum, and Jürgen Becker. 2024. A Dynamically Pipelined Dataflow Architecture for Graph Convolutions in Real-Time Event Interpretation. In *2024 IEEE 37th International System-on-Chip Conference (SOCC)*. IEEE, 1–6.

- [38] Michael A. Nielsen and Isaac L. Chuang. 2023. Quantum Computation and Quantum Information. Cambridge University Press.
- [39] Josias Old and Manuel Rispler. 2023. Generalized belief propagation algorithms for decoding of surface codes. Quantum 7 (2023), 1037.
- [40] Keshab K Parhi, C-Y Wang, and Andrew P Brown. 2002. Synthesis of control circuits in folded pipelined DSP architectures. IEEE Journal of Solid-State Circuits 27, 1 (2002), 29–43.
- [41] Lukas Postler, Sascha Heußen, Ivan Pogorelov, Manuel Rispler, Thomas Feldker, Michael Meth, Christian D Marciniak, Roman Stricker, Martin Ringbauer, Rainer Blatt, et al. 2022. Demonstration of fault-tolerant universal quantum gate operations. Nature 605, 7911 (2022), 675–680.
- [42] Zhiqiang Que, Hongxiang Fan, Marcus Loo, He Li, Michaela Blott, Maurizio Pierini, Alexander Tapper, and Wayne Luk. 2024. LL-GNN: Low latency graph neural networks on FPGAs for high energy physics. ACM Transactions on Embedded Computing Systems 23, 2 (2024), 1–28.
- [43] Victor Sanh, Thomas Wolf, and Alexander Rush. 2020. Movement pruning: Adaptive sparsity by fine-tuning. Advances in neural information processing systems 33 (2020), 20378–20389.
- [44] Mingjie Sun, Zhuang Liu, Anna Bair, and J Zico Kolter. 2023. A simple and effective pruning approach for large language models. arXiv preprint arXiv:2306.11695 (2023).
- [45] Boris M Varbanov, Marc Serra-Peralta, David Byfield, and Barbara M Terhal. 2025. Neural network decoder for near-term surface-code experiments. Physical Review Research 7, 1 (2025), 013029.
- [46] Savvas Varsamopoulos, Koen Bertels, and Carmen G Almudever. 2020. Decoding surface code with a distributed neural network-based decoder. Quantum Machine Intelligence 2 (2020), 1–12.
- [47] Suhas Vittal, Poulami Das, and Moinuddin Qureshi. 2023. Astrea: Accurate quantum error-decoding via practical minimum-weight perfect-matching. In Proceedings of the 50th Annual International Symposium on Computer Architecture. 1–16.
- [48] Yue Wu, Namitha Liyanage, and Lin Zhong. 2025. Micro blossom: Accelerated minimum-weight perfect matching decoding for quantum error correction. In Proceedings of the 30th ACM International Conference on Architectural Support for Programming Languages and Operating Systems, Volume 2. 639–654.
- [49] Yilun Xu, Gang Huang, Jan Balewski, Ravi Naik, Alexis Morvan, Bradley Mitchell, Kasra Nowrouzi, David I Santiago, and Irfan Siddiqi. 2021. QubiC: An open-source FPGA-based control and measurement system for superconducting quantum information processors. IEEE Transactions on Quantum Engineering 2 (2021), 1–11.
- [50] Bingyi Zhang, Hanqing Zeng, and Viktor Prasanna. 2022. Low-latency mini-batch gnn inference on cpu-fpga heterogeneous platform. In 2022 IEEE 29th International Conference on High Performance Computing, Data, and Analytics (HiPC). IEEE, 11–21.
- [51] Hongkuan Zhou, Bingyi Zhang, Rajgopal Kannan, Viktor Prasanna, and Carl Busart. 2022. Model-architecture co-design for high performance temporal gnn inference on fpga. In 2022 IEEE International Parallel and Distributed Processing Symposium (IPDPS). IEEE, 1108–1117.